Brain Stimulation 12 (2019) 275–289

Contents lists available at ScienceDirect

Brain Stimulation

journal homepage: http://www.journals.elsevier.com/brain-stimulation

Relation between the electric field and activation of cortical neurons in transcranial electrical stimulation

Hyeon Seo, Sung Chan Jun*

School of Electrical Engineering and Computer Science, Gwangju Institute of Science & Technology, South Korea

ARTICLE INFO

Article history:
Received 29 June 2018
Received in revised form
3 October 2018
Accepted 6 November 2018
Available online 10 November 2018

Keywords:
Noninvasive brain stimulation
Transcranial electrical stimulation
Multi-scale modeling
Finite element method
Pyramidal neuron

ABSTRACT

Background: To address the brain areas and circuits affected by transcranial electrical stimulation (tES), which had been used widely to treat psychiatric and neurological diseases, the stimulus-induced electric field in the cortex was calculated using a head model that reflects anatomical information. To obtain detailed information at the macroscopic and microscopic levels, multi-scale modeling was proposed that integrates the head model with multi-compartmental models of cortical neurons.
Objective: Our goal was to use multi-scale modeling to describe the relation between the stimulus-induced electric field and neuronal responses during tES.
Methods: We simulated sub- and supra-threshold neuronal responses to stimulus-induced uniform and realistic electric fields. For the realistic electric field, multi-scale models that combined the head model derived from structural MRIs and multi-compartmental models of neurons were constructed. Then, we simulated the steady-state membrane polarization for sub-threshold stimulation and the excitation threshold for supra-threshold stimulation by varying the tES montages. The electric field calculated was decomposed into two orthogonal components, the radial and tangential fields, which were compared to the neuronal responses.
Results: The stimulus-induced electric field depended strongly on stimulus parameters, and neuronal excitability showed a higher correlation with the radial field. We demonstrated that neurons exhibited linear polarization during sub-threshold stimulation depending on the local radial field intensity that resulted in a significant relation regardless of the tES montage. Supra-threshold stimulation showed a stronger relation with the radial field, but rather complex patterns of excitation thresholds depending on neurons' morphological features.
Conclusion: Our results indicated that cortical neurons are affected greatly by the relative direction of the stimulus-induced electric field, which may be a necessary step toward a detailed understanding of tES' potential mechanisms.

Introduction

Noninvasive brain stimulation (NIBS) has been applied widely in neuromodulation and potential treatment of a variety of neurologic and psychiatric disorders [1]. Transcranial electrical stimulation (tES) is among the noninvasive techniques that can modulate cortical excitability through electrodes attached to the scalp [2]. Like electroconvulsive therapy, tES that induces supra-threshold stimulation causes neuronal activation directly, while low intensity tES, which includes transcranial direct current stimulation (tDCS), allows sub-threshold stimulation that influences spontaneous neuronal activity. Over the past decade, NIBS has attracted interest rapidly because of its ability to treat a wide range of psychiatric and neurological disorders [1–3]; however, despite the growing attention it has received and its increased applications, uncertainty remains with respect to the brain areas affected and relevant cellular mechanisms.

Most computational studies have reported the spatial distributions of the electric field (EF) or current density with anatomical considerations using a head model derived from magnetic resonance imaging (MRI) to interpolate cellular targets with simulated EF [4–12]. Researchers have attempted to predict the brain regions (NIBS influences) that exhibit higher field strength in the cortex.

* Corresponding author. Cheomdangwagi-ro 123, Buk-gu, Gwangju, 61005, South Korea.
E-mail address: scjun@gist.ac.kr (S.C. Jun).

https://doi.org/10.1016/j.brs.2018.11.004
1935-861X/

The premise of this interpolation approach is that local polarization in a target area is proportional to the local EF magnitude, referred to as the quasi-uniform assumption [13], which presumes a uniform EF within the local area of the cortex relative to the neurons' scale, because the NIBS stimulator (for example, electrodes for tES) is situated far from the cortex [14,15]. Another way to relate EF to neuronal excitability is to calculate the second spatial derivative of the potential, referred to as the activating function [16,17]. Although these studies have supported the supposition that stimulus-induced EF is invoked in the neurophysiological response to tES, the cellular effects depend not only on stimulus parameters, but also on neurons' morphological and electrical properties. Thus, there is a large degree of unpredictability in the relation between EF and neuronal excitability.

As cellular targets of tES may help provide a more detailed understanding of underlying mechanisms and determine the optimal stimulation montage, a multi-scale model was proposed recently to provide macroscopic and microscopic details by simulating not only the stimulus-induced EF, but neuronal excitability as well. This model is constructed using the following two-step process [18,19]:

1) The head model is used to calculate a realistic NIBS-induced EF. Rather than constructing the head model, the stimulus-induced EF can be assumed to be uniform for tES based on the quasi-uniform assumption [13,15,20].
2) The EF achieved in step 1 is applied to neuronal models to simulate membrane polarizations.

Therefore, the multi-scale model for tES represents a combination of the stimulus-induced EF and compartmental models of cortical neurons. In addition, the multi-scale models that couple neuronal models with the head model and consider anatomical information may help extrapolate acute tES neuromodulation patterns from simulated cellular targets. For example, in a microscopic scale analysis, several fibre pathways were constructed in the head model via tractography and the activating function along the fibre was computed to obtain further insight into montage selection [21–23]. For detailed investigation, researchers have constructed multi-scale models using morphologically reconstructed models of cortical neurons virtually within the head model [19,24–28]. Then, they studied the neural tissue activated, the effect of different neuron types, and compartmental-specific polarizations attributable to stimulus-induced EF. Despite its significant modeling advances, multi-scale modeling remains an area of ongoing research because it is technically difficult to combine neuronal models reconstructed morphologically with the head model, which has a complex cortical geometry in the infolding and gyri. Thus, individual neuronal models usually are considered and are constructed largely in a restricted area in the head model, such as the motor cortex.

These simulation studies may help predict tES′ effect by identifying target areas and corresponding neuronal activations that the physical properties of the stimulator and combinations of stimulator placements determine [4,29]. Using the advantages of simulation studies, which allow cost-effective predictions of large combinations of parameters, researchers can choose an optimal stimulus montage and even propose a new montage using simulated EF [4,30]. Further, the spatial accuracy of simulated EF that may be applied in a neuronavigation system is achieved by increasing the realism of modeling studies, such as the model geometry and electrical properties [5–7]. Multi-scale modeling represents a powerful technique to estimate not only the spatial distribution of stimulus-induced EF, but also cellular targets' neuronal responses. However, despite the detailed analysis of multi-scale modeling approaches at the cellular level, the relation between the stimulus-induced EF and corresponding neuronal excitability in multi-scale modeling remains unaddressed.

Our goal here was to determine the relation between the stimulus-induced field and neuronal excitability with sub- and supra-threshold tES stimulation, and then investigate the way the stimulus-induced EF can be applied to interpret neuronal excitability directly and to understand tES′ outcomes at the cellular level better. In addition, we investigated neuronal excitability induced by uniform and realistic EFs to determine whether the neuronal responses induced by uniform EF could be extended to realistic EF. The realistic EF was calculated via multi-scale modeling using the anatomically realistic head model combined with multi-compartmental models of cortical neurons, details of which were provided previously [19]. Many studies have investigated the neuronal excitability under uniform EF both experimentally and computationally [15,20,31,32]. However, realistic EF may induce different neuronal responses compared to uniform EF, because the head model, which includes complex cortical folding, produces region-specific directional EF. Thereafter, the simulation results may be fed into a multi-scale model to determine tES' cellular targets and underlying mechanisms. We modeled three established neurons of stellate cells, layer 3 (L3) and layer 5 (L5) pyramidal neurons (PNs), and stellate cells and L3 PNs were distributed to cover the entire area of the cortex to generalize the neuronal excitability to cortical areas other than the motor cortex. Then, by varying tES montages, we analyzed the neuronal excitability relative to EF, which is a key component needed for a detailed understanding of cortical excitability.

Methods

We developed a multi-scale computational model that combined multi-compartmental neuronal models with different morphologies and two types of simulated EF, uniform and realistic, calculated using the head model for tES. We then considered sub- and supra-threshold stimulations by increasing stimulus amplitude, and investigated steady-state membrane polarizations for sub-threshold stimulation and excitation thresholds that have a minimum stimulus amplitude necessary to evoke an action potential for supra-threshold stimulation. We considered the hand knob region as the target area (region of interest: ROI; see Supplementary Figure S1 for detailed geometry of the ROI) when we calculated the realistic EF using the head model. Three different tES montages were considered to induce realistic EF, as shown in Fig. 1: conventional tES (C-tES) using patch-type electrodes in which either the center or the edge of an active electrode was placed on the ROI, and high-definition tES (HD-tES) that used disc-type electrodes.

Head modeling

An anatomically realistic head model that reflected precise anatomy was constructed to calculate a realistic EF for NIBS. Surface meshes consisting of five layers (white matter, gray matter, cerebrospinal fluid (CSF), skull and scalp) were obtained using an exemplar dataset of MR images SimNIBS v 1.1 provides [7,33]. Briefly, the example dataset of MR images included four images as T1-weighted and T2-weighted images with and without fat suppression. Then, following the SimNIBS pipeline, the white and gray

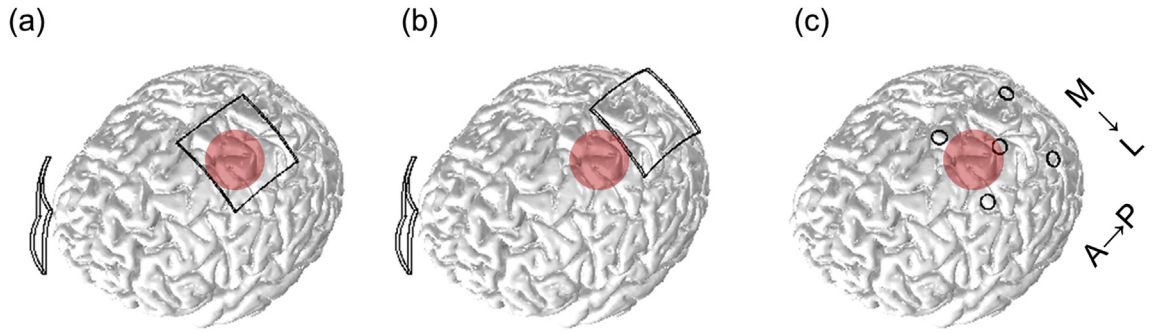

Fig. 1. Three different tES montages targeting the hand knob region. We designated the region of interest (ROI) as the hand knob area, as indicated by the red circle and used three tES montages: C-tES, where the center (a, C-tES) or edge (b, C-tES$_{edge}$) of the active electrode was placed on the ROI, and HD-tES (c). (For interpretation of the references to color in this figure legend, the reader is referred to the Web version of this article.)

matters were segmented using FreeSurfer [34,35], and the segmentation of the CSF, skull, and scalp was based on FSL BET and BETSURF [36]. The initial surface meshes were modified by custom-written functions in SimNIBS using MeshFix, such that optimal meshes that modified self-intersections or intersection between neighboring surfaces were obtained.

We generated two types of electrodes, the patch- and disc-type, for C-tES and HD-tES, respectively, which were attached to the scalp surface mesh using a custom-developed code implemented in MATLAB (2013b, The Mathworks, Inc. Natick, MA, USA) using iso2mesh [37], in ways similar to those described in Saturnino et al. [8], as follows:

- First, we determined the nodes that comprised the edge of the electrode on the scalp and then the neighboring nodes were shifted to the nodes comprising the electrode edge.
- Second, the nodes comprising the edge and the inner points of the electrode were duplicated along the normal vector to the skin surface for the electrode surface mesh.
- Third, we filled the electrode surface mesh using additional nodes that comprised the electrode.
- Finally, we used "surf2mesh" function in iso2mesh [37] based on TetGen [38] to fill the surface meshes of the head model, including the electrodes, with tetrahedral meshes that included approximately 11 million tetrahedrons.

Fig. 1 depicts the three different tES montages. For C-tES, two $5 \times 5\,cm^2$ patch-type electrodes 2 mm thick were modeled with the active electrode over the ROI (the hand area) and the reference electrode over the right supraorbital region. In addition, as EF is higher under the electrodes near the edge [9,39,40], we moved the active electrode slightly, such that its edge was placed above the target area in the same location as that of the reference electrode, referred to as C-tES$_{edge}$. For HD-tES, disc-type electrodes (radius = 4 mm; height = 1 mm) and CCNY-4 gels (height = 2 mm) were modeled according to the 4×1 montage, which included an active center electrode surrounded by four reference electrodes, with the distance between the active and reference electrodes set to 3 cm [5]. The final tetrahedral meshes of the head model had various element sizes over layers - an average of 1.67 mm^3 in the scalp, 0.07 mm^3 in the skull, 0.12 mm^3 in the CSF, 0.11 mm^3 in the gray matter, 0.24 mm^3 in the white matter, 0.78 mm^3 in the patch-type electrodes, and 0.16 mm^3 in the disc-type electrodes. In each layer of the head model, we assigned isotropic electrical conductivity obtained from the literature [5,41,42], the values of which are listed in Table 1. The Laplace equation $\nabla\cdot(\sigma\nabla V) = 0$ (V: potential field; σ: electrical conductivity) was solved via the finite element method implemented in COMSOL Multiphysics (v 5.2a, COMSOL, Inc., Burlington, MA, USA) using the conjugate gradient with preconditioning of an algebraic multigrid (a relative tolerance of 1×10^{-6}). The boundary conditions were applied to the exposed surface of the active electrode (V = constant) and the reference electrode (V = 0), and the remaining external boundaries of the scalp were set as an electrical insulator. Finally, we readjusted the stimulus amplitude to achieve a constant current stimulation of 1 mA through the active electrode.

Multi-scale modeling using the uniform EF

To determine the neuronal morphology's influence on their responses evoked by simulated EF, we used an established model of layer 4 stellate cells and L3 and L5 PNs [43] using the NEURON simulation software [44]. The neuronal models' electrical properties were unchanged from the original models and neuronal models with different morphologies shared the same channel types and densities. We then lengthened the dendrites by 60% and the diameter of the soma and geometries of the axon were modified to accommodate the dimensions of the human motor cortex [45]. We assumed that layer 4 stellate cells and L3 PNs were located within the cortex and had the same geometries as the soma (diameter: 29.8 μm) and axon (length: 1.313 mm), but not the dendrites. L5 PNs had a long axon (10.1 mm) with a soma diameter of 25 μm, because the axons of L5 PNs stretched across the boundary between the gray matter and white matter. The neuronal models consisted of a series of compartments (sections) connected by resistors and one or more segments represented each section. The neuronal model's internal voltage was defined at the center of each segment. Thus, we modulated the three-dimensional coordinates of the center points of each neuronal model and aligned the neuronal models' coordinates with the y-axis, as shown in Fig. 2.

To generate uniform EF, we developed a three-dimensional rectangular cuboid model with dimensions of 20 mm × 30 mm × 10 mm to cover all neuronal models. We then generated uniform EF directed radially or tangentially, as depicted in Fig. 2, and readjusted the stimulus amplitude to establish a constant uniform EF of 1 mV/mm. All neuronal models were combined virtually with a cuboid model and each center point of the soma of each neuronal model was located at the center of the cuboid model. Then, we calculated the extracellular potential field at each center point of each compartment of the neuronal models from the simulated uniform EF, and NEURON's extracellular mechanism was used to apply uniform EF directed radially or tangentially to the neuronal models. We simulated a steady-state somatic polarization by increasing the magnitude of uniform EF from −20 mV/mm to 20 mV/mm and determined the excitation threshold for each neuronal model.

Table 1
Tissue conductivities.

Tissue compartment	Electrical conductivity (S/m)
Scalp	0.465
Skull	0.01
CSF	1.654
Gray matter	0.276
White matter	0.126
Path-type electrode (the sponge soaked in saline solution)	1.40
Disc-type electrode	5.8×10^7
Gel	0.30

Multi-scale modeling using the realistic EF

Details of the multi-scale modeling that combined the anatomically realistic head model and neuronal models for tES [28,46] were described previously (shown schematically in Fig. 3). We modeled L4 stellate cells, and L3 and L5 PNs used in multi-scale modeling with a uniform EF. Because PNs are known to be oriented largely perpendicular to the cortical surface [47,48] and L3 PNs terminate in layer 5/6 within the cortex, the principal axis of L3 PNs was aligned according to the normal vector of the triangular element comprising the gray matter surface. To determine the neuronal models' morphological effect, we superimposed L4 stellate cells onto L3 PNs such that they shared the soma and axon, but not the dendrites. Thus, we modeled 131,958 L4 stellate cells and L3 PNs, respectively, under each triangular element comprising the gray matter surface to cover all areas of the cortex. L5 PNs have long axons that stretch to the white matter and bend in the direction of the internal capsule after crossing the boundary between the gray matter and white matter. Thus, L5 PNs were modeled in the restricted region of the cortex with axons that run straight in the same direction within the white matter (Fig. 3(b)). Here, we modeled 2006 L5 PNs in the ROI.

For sub-threshold stimulation, we simulated the steady-state transmembrane voltage responses to a stimulus-induced potential field calculated in the head model with a 1 mA stimulus amplitude. The extracellular potential field at each center point of each compartment of the neuronal models was calculated in the head model and applied to neuronal models to simulate extracellular stimulation. Then, as the PNs polarize in a compartmental-specific manner [20], in this work we simulated not only somatic polarizations, but also other compartments' polarizations (apical and basilar dendrites, initial segment of the axon, middle and terminal parts of the axon of L4 stellate cells and L3 PNs, axon bends, and near the gray and white matter boundary for L5 PNs). To simulate supra-threshold stimulation that could evoke propagation of an action potential in the neuronal models, the extracellular potentials were applied in 100 ms monophasic pulses by scaling the magnitude of the potential field that was calculated in the head model with a 1 mA stimulus amplitude up to 1000 mA. Thus, we measured the excitation threshold, which was the minimum stimulus amplitude needed to evoke action potentials in the neuronal models.

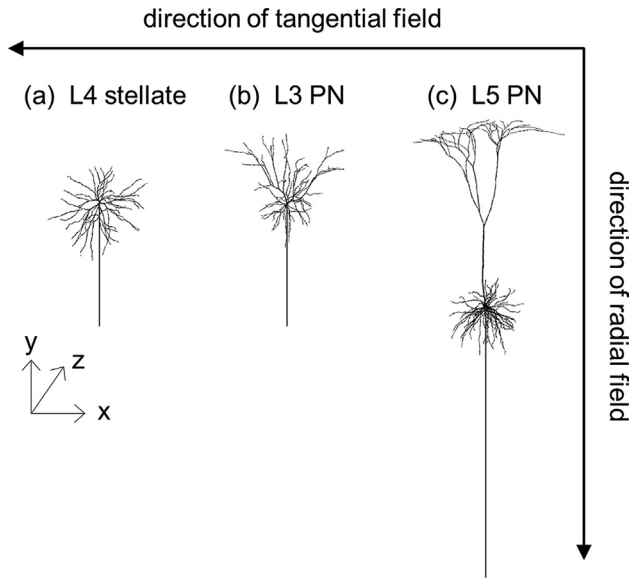

Fig. 2. Neuronal models with different morphologies: (a) layer 4 (L4) stellate cells; (b) layer 3 (L3) pyramidal neurons (PNs), and (c) layer 5 (L5) PNs. We introduced a uniform electric field that flowed parallel (radial)/orthogonal (tangential) to the somatodendritic axis.

Data analysis

For the head model, we measured the EF magnitude, which is considered typically in simulation studies. In addition, the directional component of the EF that flowed normal (radial field: RF) and parallel (tangential field: TF) to the cortical surface was analyzed; each value was calculated as RF = $\vec{E} \cdot \vec{n}$ and TF = $\vec{E} \times \vec{n}$, where $\vec{E}$ is the induced EF and $\vec{n}$ is the normal vector of the closest triangular element of the gray matter surface. We then analyzed the 1) strength and 2) the fraction of the gray matter ROI exceeding the threshold (strength) of stimulation as follows [8]:

1) The field magnitude (|EF|, |TF|, and |RF|) was calculated according to the 80th and 90th percentiles either at the cortex or the ROI.
2) We measured the fraction of the ROI that exceeded the given strength of stimulation, which was the 80th or 90th percentiles of field magnitude at the cortex. The higher values (near 100%) indicate that the highest field magnitude occurred in the ROI, i.e., the stimulation was focused in the ROI. The lower values (near 0%) indicate the highest field occurred outside the ROI (other areas in the cortex).

We calculated the Pearson correlation coefficient (PCC) between the neuronal models' field magnitude and polarization. For RF, positive values indicated that the field direction flowed inward and negative values indicated that it was directed outward from the superficial to lower cortical layers. Thus, for sub-threshold stimulation, the correlation between RF and the neuronal models' polarization (not absolute value) determined whether positive or negative RF related to depolarization or hyperpolarization. We considered the absolute value of neuronal polarization for the magnitude of EF and TF (|EF|, and |TF|). For supra-threshold stimulation, we calculated the PCC between the field magnitude (|EF|,

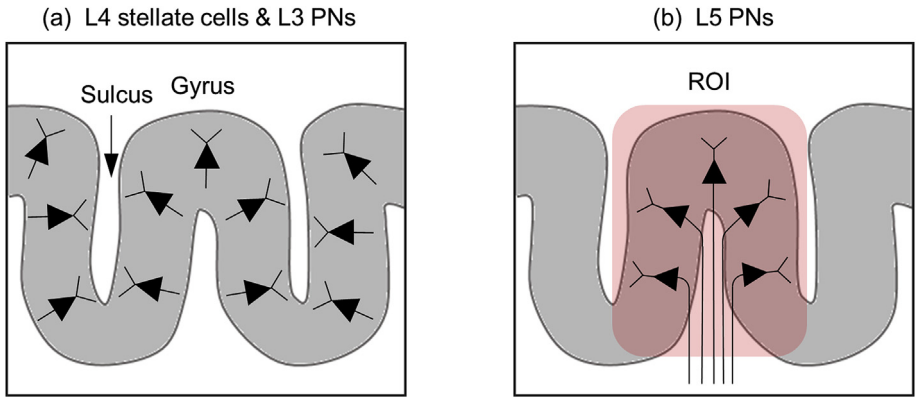

Fig. 3. Schematic showing distribution of L4 stellate cells, and L3 (a), and L5 PNs (b). Note that L5 PNs are distributed in the ROI, while L4 stellate cells and L3 PNs are distributed over the entire area of the cortex.

|TF|, and |RF|) and excitation thresholds where neuronal models showed activation under 1000 mA stimulus amplitude.

Results

Uniform EFs' effects on neuronal models' morphology

We simulated the effects on the neuronal models of uniform EF directed radially (uniform radial field; uniform RF) and uniform EF directed tangentially (uniform tangential field; uniform TF: Fig. 2). The neuronal models' steady-state polarizations were quantified for sub-threshold stimulation (−20 mV/mm to 20 mV/mm uniform fields: Fig. 4) and we found linear polarizations when uniform RF/TF increased. The membrane polarization throughout each neuronal model largely was depolarized with anodal stimulation (positive EF) and hyperpolarized with cathodal stimulation (negative EF). However, the stellate cells showed opposite polarizations at the soma, with depolarization with negative RF and hyperpolarization with positive RF (Fig. 4(a)). The axon terminals of stellate cells and L3 PNs were polarized comparably for uniform RF because

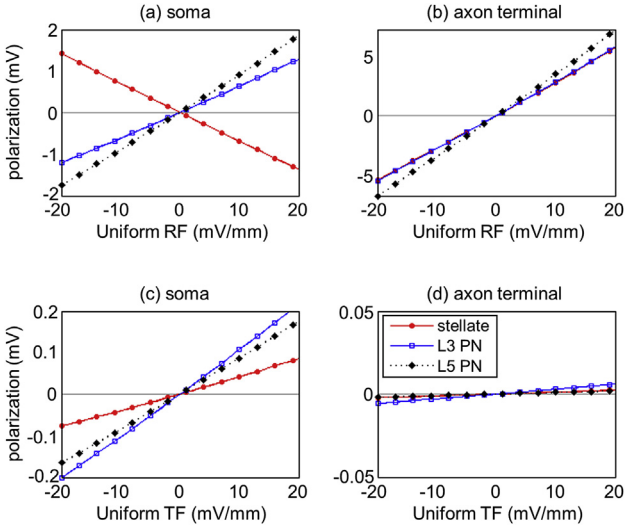

Fig. 4. Neuronal polarization with respect to sub-threshold uniform EF. The steady-state polarizations at the soma and axon terminal of the stellate cells, L3 PNs, and L5 PNs were simulated according to a uniform EF (uniform RF; a and b) directed radially, and uniform EF directed tangentially (uniform TF; c and d). The incremental magnitude of uniform RF/TF polarized the soma and the axon terminal linearly.

their axons have the same electrical properties and morphologies. Uniform TF polarized the soma and the axon terminal linearly, but had a nominal influence compared to the radial RF (Fig. 4(c and d)).

We calculated the excitation threshold that could evoke action potentials in the neuronal models by increasing the magnitude of uniform EF. For uniform RF, the threshold was 33 mV/mm, 32 mV/mm, and 37 mV/mm for the stellate cells, L3 PNs, and L5 PNs, respectively. The threshold was significantly higher for uniform TF: 138 mV/mm, 91 mV/mm, and 135 mV/mm for stellate cells, L3 PNs, and L5 PNs, respectively, because of uniform TF's reduced effects on neuronal polarizations. Under uniform EF, we found variability in neuronal polarizations and excitation thresholds invoked throughout each neuronal model with respect to the direction of EF, and speculated that it is important to use realistic EF calculations relative to the neurons' orientation that underpin modeling multi-scale models using the anatomically realistic head model.

Sub-threshold tES' effects on neuronal polarizations

Fig. 5 depicts the distributions of field strength and somatic polarization of stellate cells and L3 PNs on the cortical surface for the three different montages of sub-threshold tES. For sub-threshold stimulation, we applied a 1 mA stimulus amplitude through the active electrode. For C-tES and C-tES$_{edge}$, which used the patch-type electrodes, we observed diffused cortical field strength and higher field strength in areas distinct from the active electrode. High TF areas were restricted largely to the top of the gyrus, while high RF was focused on the wall of the gyrus in the areas beyond the electrodes' placement. The C-tES$_{edge}$, which was proposed to improve the field strength in the ROI through the edge effect, showed greater magnitudes of EF and TF in the ROI compared to those in C-tES (Supplementary Figure 1). In addition, |EF| and |TF| were focused on the top of the gyrus in C-tES$_{edge}$, but on the wall of the gyrus in C-tES. However, the RF distribution in both C-tES and C-tES$_{edge}$ showed a comparable magnitude focused on the top of the gyrus. Although the three montages selected targeted the ROI (the hand area), HD-tES showed higher focality in the ROI than did C-tES and C-tES$_{edge}$. The RF spatial distributions showed patterns consistent with L3 PNs' polarization, such that there were positive (negative) values of RF-related depolarization (hyperpolarization) in L3 PNs, while stellate cells showed opposite polarization patterns to those of the RF spatial distributions that resulted in depolarization for negative RF, and hyperpolarization for positive RF.

We then calculated the PCC to investigate the relation between the field strength and the neuronal models' somatic polarization

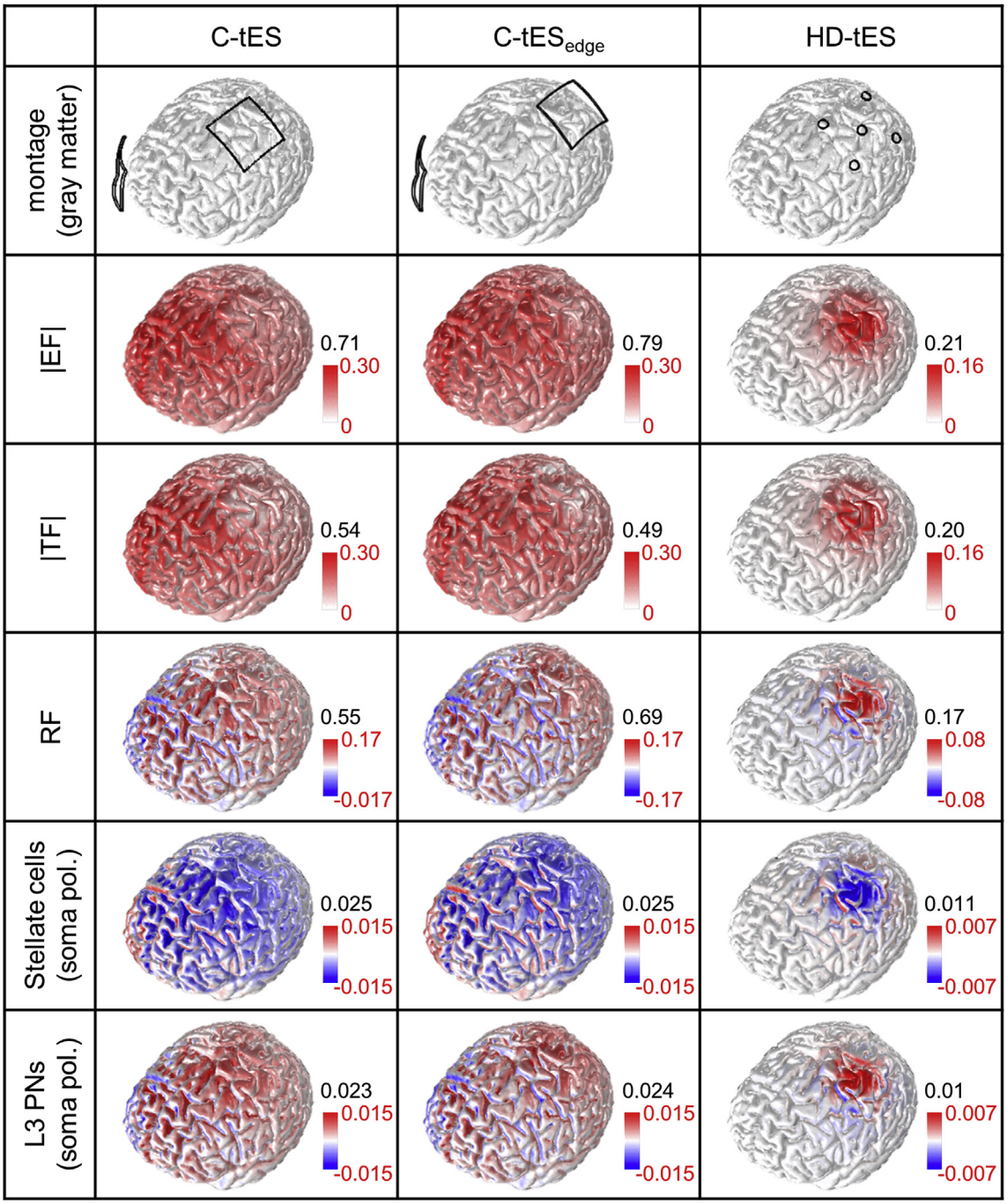

Fig. 5. The spatial extent of EFs (V/m) and somatic polarization (mV) of stellate cells and L3 PNs induced by the three different tES montages. The spatial distributions of the magnitude of EF and TF (|EF| and |TF|). For the RF distribution, red (blue) indicates the inward (outward) direction from the superficial to lower cortical layers. In addition, the spatial extent of somatic polarizations (soma pol.) of stellate cells and L3 PNs distributed on the cortex are shown. The color scale of the cortical surface view is adjusted according to the bottom value (red) of the range bar for better visualization. The top value (black) of the range bar indicates the maximum value of the field magnitude and somatic polarization. (For interpretation of the references to color in this figure legend, the reader is referred to the Web version of this article.)

(Fig. 6). While both uniform RF and TF polarized neurons linearly (Fig. 4), only realistic RF showed a higher correlation with neuronal polarizations regardless of the neuronal morphologies and the tES montages used. Consistent with previous findings for stellate cells, that uniform RF resulted in hyperpolarization in positive field strength and depolarization in negative field strength, stellate cells were correlated negatively with RF. When we focused on the correlation between somatic polarization and |EF|, which has been exploited widely in simulation studies, C-tES and C-tES$_{edge}$ showed negligible values of PCC in the ROI because of the diffused cortical EF that was concentrated in areas far from it, while in contrast, HD-tES showed higher PCCs because of the focalized field distributions. In the ROI, |TF| in C-tES and C-tES$_{edge}$ was correlated negatively with neurons' somatic polarization, because higher RF and TF areas did not overlap in the ROI (Supplementary Figure S2) and somatic polarization had a higher correlation with RF.

Regardless of neuronal morphologies, somatic polarization throughout each neuron showed higher correlations with RF and all

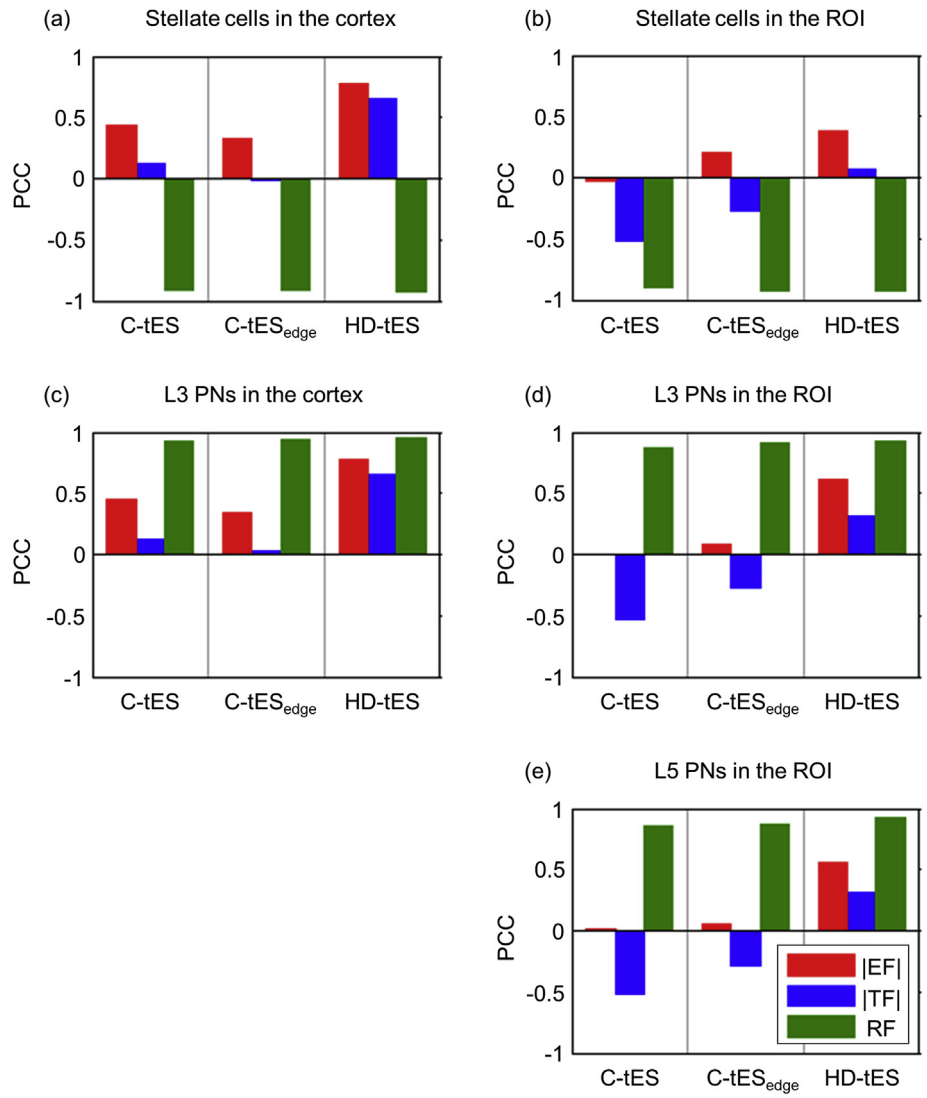

Fig. 6. The correlation coefficient between EFs and somatic polarization of neurons tES produced. We calculated the PCCs between field strength and somatic polarization of stellate cells (a and b), L3 PNs (c and d), and L5 PNs (e) distributed over the entire area of the cortex (a and c) or on the ROI (b, d, and e). Note that the RF's value approximates ±1, indicating a higher (positive or negative) correlation between RF and somatic polarization of stellate cells, and L3 and L5 PNs.

the compartments of neurons (including dendrites and the axon) were related consistently and profoundly to RF. According to neurons' compartmental-specific polarizations, we observed apical dendritic hyperpolarization associated with depolarization of basilar dendrites, in which the RF was correlated negatively with apical dendrites and positively with basilar dendrites. The absolute value of PCC between RF and polarization was approximately 0.80 or more in all compartments of stellate cells and L3 PNs, regardless of the montage, and thus all compartments showed a higher relation with RF. In contrast, L5 PNs showed compartmental-specific correlation. Thus, RF's effect on L5 PNs decreased far from the soma and the field strength on the cortical surface did not affect the terminal part of the axon (Supplementary Figure S3).

Generally, a higher strength EF is observed with greater distance between electrodes [49,50]. Consistently, we observed that using pad electrodes produced higher field strength in the cortex compared to that in HD-tES (Table 2). For example, C-tES and C-tES$_{edge}$ showed consistent field strength throughout the cortex that was 9 times higher $|EF|_{90th}$ than that in HD-tES. However, when we focused on the ROI, these discrepancies between C-tES and HD-tES decreased, such that they showed comparable RF strength and somatic polarization. This reflected higher focality in HD-tES, while C-tES resulted in a diffused field distribution and higher field strength at sites distinct from electrodes. Consistently, L5 PNs showed slightly higher 80^{th} and 90^{th} percentiles of somatic polarization in the ROI in C-tES and C-tES$_{edge}$ than in HD-tES. Further, C-tES$_{edge}$ showed a greater EF magnitude in the ROI compared to C-tES, but the strength of RF was comparable between C-tES$_{edge}$ and C-tES, such that they induced a similar polarization strength in neurons in the ROI.

The higher value of the fraction of the gray matter ROI that exceeded the threshold, which indicated the higher field was focused in the ROI, was confirmed for HD-tES (Table 3). HD-tES showed a perfect concentration of EF in the ROI ($EF_{80th} = 100\%$)

Table 2
Stimulation intensity. The three different tES montages' effects on the 80th and 90th percentiles of the field strength (V/m) and somatic polarization of stellate cells and L3 PNs (μV).

		C-tES		C-tES$_{edge}$		HD-tES	
		Cortex	ROI	Cortex	ROI	Cortex	ROI
Field strength (V/m)	$\|EF\|_{90th}$	0.18	0.14	0.18	0.19	0.02	0.14
	$\|EF\|_{80th}$	0.15	0.13	0.16	0.17	0.01	0.13
	$\|RF\|_{90th}$	0.12	0.10	0.12	0.09	0.01	0.06
	$\|RF\|_{80th}$	0.08	0.06	0.09	0.08	0.005	0.04
somatic polarization (μV)	$\|$stellate pol$\|_{90th}$	8.00	8.20	8.40	9.20	0.70	6.50
	$\|$stellate pol$\|_{80th}$	6.00	6.80	6.60	8.00	0.40	4.30
	$\|$L3 PN pol$\|_{90th}$	7.10	7.90	7.60	8.40	0.60	6.60
	$\|$L3 PN pol$\|_{80th}$	5.30	6.80	5.80	7.00	0.30	4.20
	$\|$L5 PN pol$\|_{90th}$	–	8.30	–	9.20	–	6.50
	$\|$L5 PN pol$\|_{80th}$	–	7.10	–	7.80	–	4.40

and the value in RF and neurons' somatic polarization was higher compared to that in C-tES and C-tES$_{edge}$. Further, C-tES$_{edge}$ showed higher EF concentration in the ROI, but comparable RF focality and neuronal somatic polarization, than did C-tES, consistent with the field strength findings that C-tES$_{edge}$ produced higher EF strength, but a similar strength for RF and somatic polarization in the ROI.

Supra-threshold tES' effects on neuronal polarizations

We calculated the excitation thresholds for stellate cells and L3 PNs on the cortical surface by increasing stimulus amplitude, which increased the extracellular potential fields calculated for sub-threshold tES to 1000 mA. As Fig. 7 shows, the excited areas that showed lower thresholds matched the spatial extent of EF in Fig. 5 generally across the different tES montages. However, although stellate cells and L3 PNs had the same electrical properties and axons, but different dendrite morphology, they showed different threshold patterns. Under uniform RF, stellate cells and L3 PNs showed comparable thresholds, but when we applied realistic EF, L3 PNs showed much lower thresholds with larger cortical activation areas than did stellate cells. In the ROI, most L3 PNs were stimulated regardless of the tES montages, while stellate cells were targeted by HD-tES well compared to C-tES and C-tES$_{edge}$.

To focus further on the ROI, we analyzed the distributions of the stellate cells', L3 PNs', and L5 PNs' thresholds in the ROI (Fig. 8). As expected by the spatial extent of the thresholds in Fig. 7, stellate cells showed higher threshold distributions in the ROI than did L3 and L5 PNs. In addition, C-tES$_{edge}$, which was proposed to target ROI efficiently, showed lower threshold distributions for stellate cells and L3 PNs compared to C-tES, consistent with the higher somatic polarization at C-tES$_{edge}$ than at C-tES (Table 2). However, L5 PNs induced the lowest threshold distributions in C-tES, largely because RF C-tES induced flowed perpendicular to the top of the gyrus in the ROI (Supplementary Figure S2) and this RF direction matched with the axon of L5 PNs after crossing the boundary between the gray and white matters (Fig. 3(b)). In addition, because L5 PNs in the white matter in the ROI have axons with paths that extend in the same direction, they were activated by a relatively lower stimulus amplitude compared to other neuronal models, regardless of the tES montage. This underscores the neuronal morphologies' importance relative to the induced EF and realistic EF's effects on neuronal models.

We calculated PCCs to compare field strengths and neurons' excitation thresholds (Fig. 9), and while RF showed a greater association with those thresholds, it had a relatively insignificant effect on neurons' activation compared to the results of neuronal polarization sub-threshold tES induced (Fig. 6). Although a greater relation between RF and neurons' thresholds was observed in general, stellate cells had a negligible PCC with RF during C-tES (Fig. 9(a)). A higher PCC with RF was observed in L3 PNs compared to stellate cells, and the PCC with RF increased in the ROI compared to the cortex. Interestingly, L5 PNs showed a negligible correlation with field strengths in the ROI (Fig. 9(e)), possibly attributable to the fixed direction of L5 PNs axons in the white matter.

Table 3
The fraction of the gray matter ROI exceeding the stimulation threshold. The ROI that exceeded the 80th and 90th percentiles of field strength in the gray matter overall was calculated for field strength (|EF| and |RF|) and somatic polarizations (stell and L3 represent stellate cells and L3 PNs, respectively). When higher field strength or somatic polarization was focalized in the ROI, the value was 100%.

	EF_{90th}	EF_{80th}	RF_{90th}	RF_{80th}	$stell_{90th}$	$stell_{80th}$	$L3_{90th}$	$L3_{80th}$
C-tES	0.58	4.49	1.20	7.92	11.84	24.66	18.09	29.67
C-tES$_{edge}$	15.95	31.70	2.85	10.00	16.42	33.34	15.06	31.45
HD-tES	99.85	100.00	66.67	80.36	75.67	85.78	77.19	87.86

Discussion

Prior modeling studies have demonstrated stimulus-induced EF that characterizes the cellular targets of brain stimulation and even have proposed optimal montages with anatomical considerations [5–7,51]. Recently, details of neuronal activation were simulated by incorporating multi-compartmental models of cortical neurons via multi-scale modeling [19,24,25]. However, macroscopic and microscopic analyses with multi-scale modeling are scarce because of modeling complexities, and the way in which stimulus-induced EF modulates neuronal excitability is not understood fully. Therefore, we investigated realistic EF's effect on neuronal excitability and measured the correlations between the stimulus-induced EF and neurons' polarization and excitation thresholds in silico. Further, we examined the utility of multi-scale modeling using realistic EF despite its intricate modeling processes.

Here, we constructed multi-scale models for tES to relate target areas extrapolated by stimulus-induced EF to cellular targets obtained through the multi-scale models, because the precise target region that can be achieved by increasing modeling accuracy may lead to a better understanding of tES' influence. In particular, we simulated both sub- and supra-threshold stimulations, because sub-threshold stimulation is known to modulate ongoing neuronal processing, while supra-threshold stimulation affects cortical neurons' activation directly [20,52,53]. We then demonstrated the way in which stimulus-induced EF influenced neurons' polarization and activations, which might provide a better understanding of which factors contribute to the modulation of PNs in both sub- and supra-threshold stimulations.

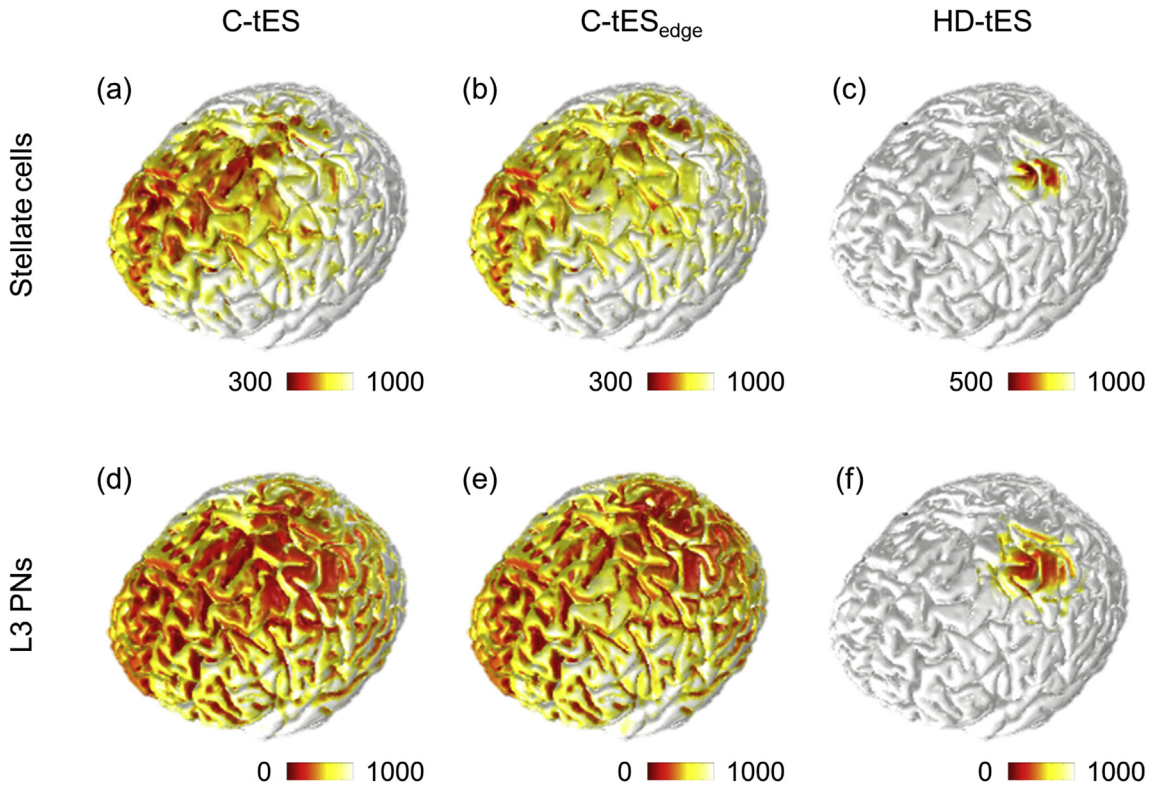

Fig. 7. Spatial extent of excitation threshold (mA) of stellate cells and L3 PNs induced by the three different tES montages. The threshold distribution of stellate cells (a, b, and c) and L3 PNs (d, e, and f) induced by C-tES (a and d), C-tES$_{edge}$ (b and e), and HD-tES (c and f). The color scale for the stellate cells is adjusted for better visualization. (For interpretation of the references to color in this figure legend, the reader is referred to the Web version of this article.)

Validity of multi-scale models

The results reported here assumed that realistic EF was nonuniform EF on the scale of single neurons. To determine whether realistic EF calculated using the head model was not uniform EF with variable field orientation, we calculated the directional derivative of |EF| using the head models as follows:

$$\nabla_{\mathrm{n}}|EF| \equiv \nabla|\mathrm{EF}| \cdot \frac{\mathrm{n}}{|\mathrm{n}|} \approx \lim_{h} \frac{EF(x+h\hat{n}) - EF(x)}{h},$$

where n is the neurons' principal direction, which is identical to their normal direction to the cortical surface. We approximated the directional derivative of |EF| as the rate at which the EF changed from a point at the dendrites' tip to a point on the axon terminal of L3 PNs; the point at the dendrites' tip was defined as that where a point aligns in the neurons' principal direction. Thus, the directional derivative of |EF| was calculated on the scale of L3 PNs. If the realistic EF calculated had a uniform field, then the value of the directional derivative of |EF| would be 0. As Supplementary Figure S4 shows, during sub-threshold stimulation, we found a higher directional derivative of |EF| distributed broadly over a large brain area in both C-tES and C-tES$_{edge}$, and focalized distributions of a higher directional derivative of |EF| in HD-tDCS. This implied that the realistic EF calculated here was a nonuniform field on the scale of single neurons.

For supra-threshold stimulation, we presented the L3 PNs' excitation threshold using the head model, assuming that the realistic EF calculated was uniform on the scale of neurons, to facilitate comparison between excitation thresholds under uniform and realistic EFs; Fig. 7 presents the excitation threshold for realistic EF and Supplementary Figure S5 depicts the excitation threshold under the uniform EF condition. Excitation thresholds of L3 PNs under the uniform EF condition were determined by the minimum stimulus amplitude that local |RF| and |TF| reached the constant excitation thresholds' value for uniform RF (32 mV/mm) and uniform TF (91 mV/mm). Excitation thresholds of L3 PNs under

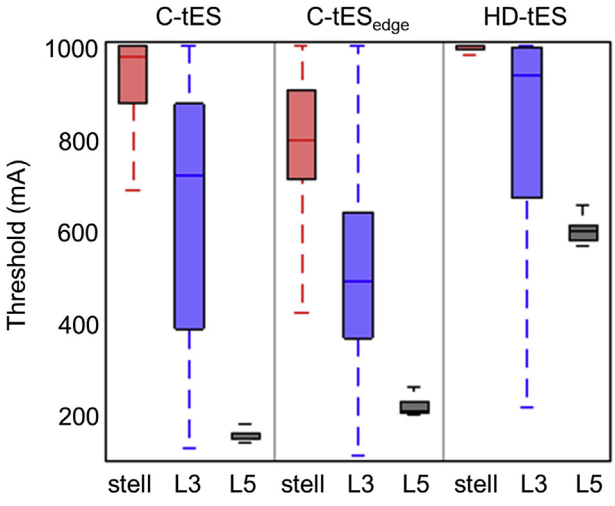

Fig. 8. Excitation thresholds of neurons in the ROI induced by the three different tES montages. To investigate tES' effects on the ROI, we focused on the thresholds of stellate cells (stell: red), L3 PNs (L3: blue), and L5 PNs (L5: black) in the ROI and then analyzed the median and the first to third quartiles spanning the central rectangles, where whiskers indicate maximum and minimum values. All pairs between neuron types and tES montages differed significantly (t-test, $p < 0.001$). (For interpretation of the references to color in this figure legend, the reader is referred to the Web version of this article.)

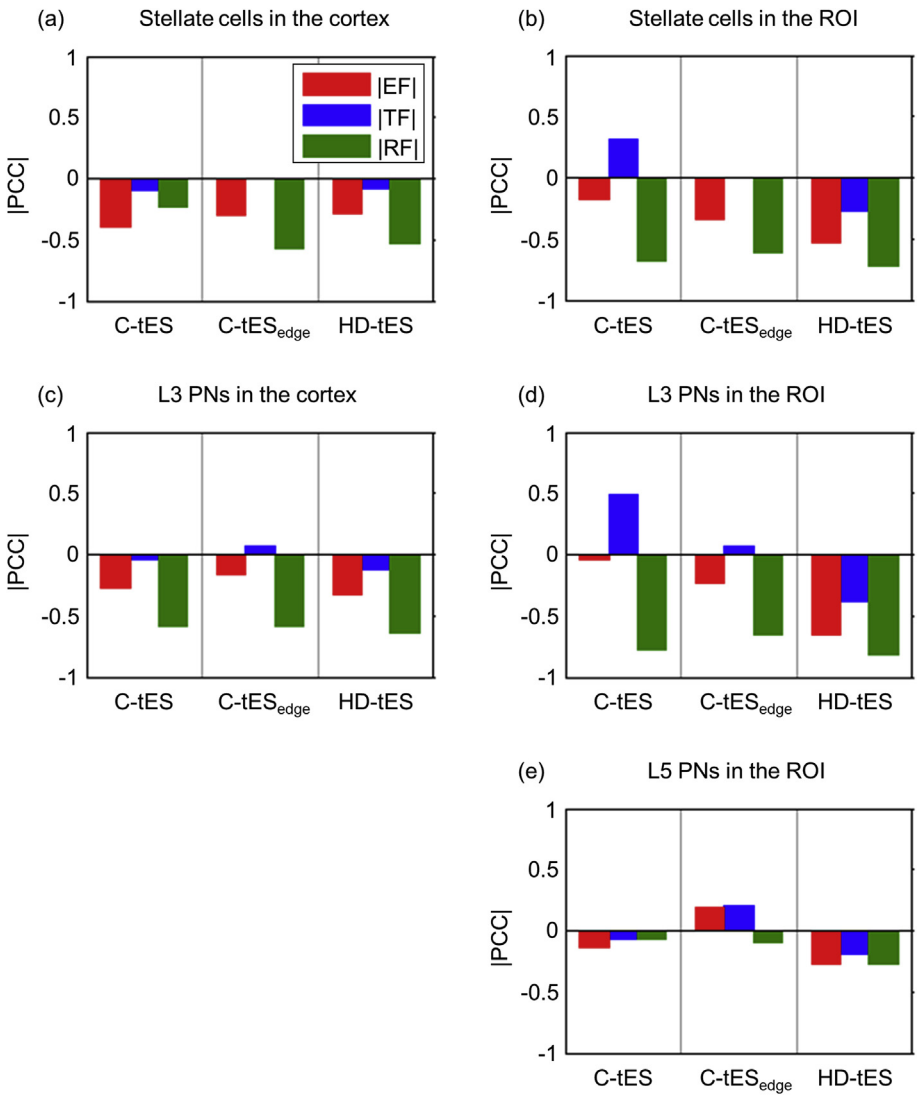

Fig. 9. Correlation coefficients between EFs and the excitation thresholds of neurons tES produced. We calculated the PCCs between field strengths (|EF|, |TF| and |RF|) and the excitation thresholds of stellate cells (a and b), L3 PNs (c and d), and L5 PNs (e) distributed over the entire area of the cortex (a and c) or on the ROI (b, d, and e). As higher field strengths induced generally lower thresholds, the correlations between field strength and thresholds largely were negative.

the uniform EF condition (Supplementary Figure S5) showed distributions comparable to those of realistic |RF| and |TF| (Fig. 5), and resulted in uniform RF condition inducing higher activations focused on the lip of the gyrus, and lower excitation thresholds for uniform TF condition focused on the top of the gyrus for tES and tES$_{edge}$. Compared to the excitation threshold with realistic EF (Fig. 7), which showed different patterns between stellate cells and L3 PNs according to their different dendritic morphologies, the excitation threshold under the uniform EF condition (Supplementary Figure S5) showed consistent patterns for stellate cells and L3 PNs that resulted in higher correlations with field distributions (>0.80). Collectively, we demonstrated the validity of multi-scale models by observing the non-uniform realistic EF on the scale of single neurons using the head models under sub- and supra-threshold stimulations.

Cortical excitability induced by sub-threshold stimulation

In this study, we attempted to address sub-threshold stimulation's effect on cortical excitability using both uniform and realistic EFs in multi-scale models. For realistic EF, we constructed three different tES montages coupled with stellate cells, L3 PNs, and L5 PNs, and then analyzed the relation between stimulus-induced EF and neurons' polarization during sub-threshold tES using the PCC. We constructed large-scale models for stellate cells and L3 PNs that were distributed on the cortex that allowed us to determine the correlation between neurons' polarization and field strength.

Under uniform EF, increasing the magnitude of RF and TF modulated neuronal polarization linearly, and, compared to TF, RF affected neuronal polarization profoundly (Fig. 4). However, for realistic EF neurons' somatic polarization showed no significant correlation with EF and TF, and the only higher correlations were between neurons' polarization and RF, regardless of the tES montage (Fig. 6). As expected, as neurons oriented radially to the cortical surface conformed to the RF direction, we observed comparable patterns between RF and neurons' polarizations. This implies the importance of neuronal orientation relative to the field induced, consistent with previous findings that EF flowing to the somatodendritic axis contributes to neuronal polarization preferentially [15,54]. Interestingly, although only part of L5 PNs' axons

within the gray matter were modeled in the direction radial to the cortical surface, they showed a stronger relation with RF and their somatic polarization compared to EF and TF. In an exploratory manner, we calculated the PCC between RF and the polarization of stellate cells and L3 PNs' specific compartments (soma, initial segment of the axon, middle, and terminal parts of the axon) and found higher PCCs (nearly 0.90) in all compartments selected. This indicated that RF affected stellate cells and L3 PNs profoundly and we could extrapolate their polarization using RF. We then considered L5 PNs, which have a long axon that stretches to the white matter and a different axonal orientation to stellate cells and L3 PNs in the ROI. The correlation between RF and somatic polarization of L5 PNs also was greater than 0.85; this effect decreased in the axons located far from the soma, and showed no correlation with the terminal part of the axon. To gain some insight about the way in which the induced field might relate to the terminal part of the axon, we determined the correlation between polarization at the L5 PNs' axon terminal and the EF that is parallel to the axon terminal locally, and found significant correlations of approximately 0.97 in all montages selected. This suggests that, under sub-threshold stimulation, all PN compartments might polarize linearly with respect to local EF, which is consistent with the quasi-uniform assumption [13].

The stellate cells and L3 PNs had the same electrical properties and axon, although not dendritic morphology, and they showed different patterns of membrane polarization under the same stimulus-induced EF, as shown in Fig. 4 for uniform EF and Fig. 5 for realistic EF. In general, positive EF is attributed to membrane depolarization, while negative EF induces membrane hyperpolarization [55,56]. This fed well into the polarization of L3 PNs and L5 PNs, as Figs. 4 and 5 show. However, stellate cells showed opposite polarization that resulted in decreased/increased excitability with positive/negative EF, and this variation in membrane polarization is consistent with Yi et al.'s findings [32], who studied the effects of PNs' morphologic features induced by sub- and supra-threshold uniform EFs. They described the asymmetric dendrites as effective sinks (dendrites close to the positive field) and sources (dendrites close to the negative field) EF caused, and thus, L3 PNs and L5 PNs had more sources and fewer sinks with positive RF that resulted in somatic depolarization. In contrast, stellate cells had fewer sources and more sinks with positive RF and thus, responded to it negatively. Through these simulations, we could speculate the effect neurons' morphologic features on their responses during sub-threshold stimulation.

TF is known to polarize neurons that extend parallel to the cortical surface and to have a minor influence on modulation of PNs' somatic polarization [20,57]. We found consistently low correlations between TF and neurons' somatic polarization (Fig. 6), and further, all of the neurons' compartments correlated weakly with TF. On the top of the gyrus in the ROI, negative TF was observed with C-tDCS and HD-tDCS, but a positive field strength was found with C-tDCS$_{edge}$ (Supplementary Figure S2). Thus, according to the degree to which neuronal polarization depends on field direction, neurons oriented parallel to the cortical surface, for example, basket cells, might show higher polarization for C-tDCS$_{edge}$ on the top of the gyrus in the ROI, and result in reversed polarization profiles for C-tDCS and HD-tDCS depending on the electrode's location, consistent with TF patterns.

Cortical excitability induced by supra-threshold stimulation

We found that the neurons' polarization was correlated with RF intensity under sub-threshold uniform and realistic EFs, and simulated neurons showed a constant threshold under uniform EF. In this study, we attempted to determine whether RF intensity can predict neuronal excitability by supra-threshold stimulation when we applied realistic EF, consistent with sub-threshold stimulation. Therefore, we assumed a negative correlation between field strengths and thresholds, and thus, lower intensity RF might require a higher threshold, while higher RF intensity might requires a lower threshold to activate neurons.

With sub-threshold stimulation, there was a nearly perfect correlation between RF and neuronal polarization, but the relation between RF and neurons' activation during supra-threshold stimulation was unclear, although RF showed the highest correlation with neurons' activation compared to EF and TF (Fig. 9). In addition, while sub-threshold stimulation uniform EF induced could be reflected in the realistic EF's results, supra-threshold stimulation that induced neuronal activation by realistic EF was correlated negligibly with neuronal responses under uniform EF. We suggest that realistic EF altered neurons' activation nonlinearly because of its different orientation relative to neurons. For example, L3 PNs had lower thresholds than did L5 PNs with uniform EF, but when we applied realistic EF, L5 PNs showed much lower thresholds in the ROI than did L3 PNs. As the field direction in the ROI matched part of the L5 PNs' axon, L5 PNs exhibited lower threshold distributions accordingly. A myriad of stimulus-induced field directions was observed in other non-motor brain areas or by varying tES montages, and the threshold distributions of L3 PNs and L5 PNs might be reversed depending upon the field direction. Further, under uniform EF, we found that the field direction affected the excitation thresholds significantly, such that TF induced neuron thresholds approximately 3–4 times higher than did RF. These simulations suggested that the EF's orientation relative to neurons plays a crucial role in determining their activation. Accordingly, neurons simulated through multi-scale modeling using realistic EF might have different thresholds, because the intensity and orientation of realistic EF varied according to the stimulus-induced EF attributable to the complex geometry of the head model and the different electrode montages, and thus led to a relatively lower correlation between neuronal thresholds and field magnitude (Fig. 9). Therefore, the use of multi-scale models using realistic EF may be favorable to investigate cellular targets of stimulation and detail neuronal responses supra-threshold stimulation induces, as regional-specific directional fields determined neuronal responses.

Neurons' morphological features affect the relation between neuronal activations and field strengths. When we compared the stellate cells and L3 PNs, which have different dendrite morphologies, they exhibited different threshold distributions (Fig. 8) and relations with field strengths (Fig. 9), while with sub-threshold stimulation, the stellate cells and L3 PNs had comparable, but inverse, polarization patterns with higher correlations. The variation in neuronal responses was not constrained to that between cell types, but occurred within cell types as well; Radman et al. [20] showed neuronal responses induced by sub- and supra-threshold uniform EFs *in vitro* and considered the cell types (inter neurons, and layer 2/3 and layer 5/6 PNs) distinct morphologic features. They found sub-threshold uniform EF polarized somatic membrane potentials linearly and different firing thresholds between and within cell types with supra-threshold stimulation. Yi et al. [32] reported the importance of neurons' morphologies in determining their responses by constructing PNs with a simple structure and realistic morphology with uniform EF in silico. Wu et al. [58] simulated electromagnetic stimulation with highly detailed morphological features of L2/3 and L5 PNs and also tested an idealized axon, which had the same morphology as that in our proposed models, by replacing the realistic axons of PNs. Through these existing observations, neuronal morphologies have been confirmed to play crucial roles in determining neuronal responses. While our modeling study incorporated stimulus-induced realistic EF, we

modeled limited morphological features of PNs. Therefore, further investigation of various morphological features of neuronal models should be considered in multi-scale models.

Limitations

Neuronal modeling limitations

In our model, we simulated neuronal excitability via neuronal models having dendrites and axons with different morphologies, and investigated the way these morphological features affected tES-induced neuronal responses. We found that stellate cells' and L3 PNs' different dendrite morphologies induced not only different polarizations during sub-threshold, but also different threshold patterns during supra-threshold stimulation. In addition to dendrite morphologies, the axon morphology affected neuronal responses profoundly, such that we found significantly lower threshold distributions of L5 PNs compared to those of stellate cells and L3 PNs, which have relatively short axons. The axon morphology of L5 PNs constructed in our model was designed by considering previous multi-scale models that combined neuronal models with the extruded slab model, which has a simple cortical geometry, for invasive cortical stimulation [45,59–61]. Determining the actual direction of the axons inside the white matter can be performed by tract estimation using diffusion tensor imaging (DTI). Previous modeling studies have constructed nerve models using the tractography-based modeling approach and then calculated EF's spatial gradient (the activating function) for magnetic stimulation [21,22,62] and tDCS [50]. Further, De Geeter et al. [24] proposed compartmentalized tractography-based nerve models composed of single dendrites, the soma, and the myelinated axon. While tractography-based nerve models provide elaborate axon architectures, they consider the activating function along the tracts using simple neuronal models. In addition, the dominant direction of L5 PNs' axons in the hand knob of the precentral gyrus in our model was very similar to that in the tractography-based nerve model [21,22], and matched tES-induced EF that flowed largely perpendicular to the gyrus (ROI). Thus, L5 PNs had lower threshold distributions than did other types of neurons. To achieve more precise information on axonal architecture and investigate neural excitability beyond superficial areas, further work should incorporate realistic neuronal morphologies using tractography.

Most multi-scale modeling studies, not just this study, have presented neuronal models that projected PNs that were oriented radially [19], because these are the most abundant neurons in the cerebral cortex and their activation evokes descending volleys, including in the corticospinal tract [63–65]. Only a few studies using the extruded slab model, which has only a simple geometry, have considered not only PNs, but also horizontal neurons in invasive cortical stimulation [59–61] and magnetic stimulation [26,66]. The extruded slab model presents the precentral gyrus, two adjacent sulci, and two neighboring gyri, and models by extruding a 2D cross-section of the model into 3D. Because of the model's simplified geometry, horizontal neurons may be modeled tangentially to the interface between the gray matter and white matter with respect to the 2D cross-section of the model. However, we presented PNs' responses induced by tES, as the constructed head model has a complex cortical geometry in the sulci and gyri, and we had limited information about the architectures of non-pyramidal cells. As stimulus-induced EF that flows longitudinally along the axon excites neurons preferentially, we expected that TF might show a relation with horizontal neurons. Although neuronal orientation relative to the induced EF may underpin the utility of tES, we found that neuronal responses depended on various parameters, such as the neurons' morphology and location and stimulus intensity (sub- or supra-threshold). Therefore, myriad types of neurons within and across excitatory and inhibitory neurons in the cortex should be considered in further modeling studies to obtain a better understanding of neuromodulation's biophysical mechanisms.

Cooperation on the part of large populations of neurons is necessary in brain functions, such as sensory processing and motor control, and NIBS is able to modulate such neuronal activities according to evidence derived from specific neural networks [1,67]. To acquire a better understanding of cortical responses, several studies have attempted to reproduce indirect wave deflections trans-synaptic neuron activation induced by developing network models that were able to reproduce epidurally-recorded responses (indirect waves) to magnetic stimulation [68,69]. In contrast, the multi-scale models proposed are limited to exploring electrical stimulation effects on single cells. However, we measured neurons' polarization related to complex patterns of EF that varied according to large combinations of tES parameters. Further, this model could be exploited to investigate the effects of neurons' relative orientation on stimulus-induced EF, which might be an important factor in determining neuronal responses [70,71]. Moreover, although the multi-scale modeling proposed described only the responses of individual PNs, detailed information at the macroscopic and microscopic levels can be integrated synergistically for further large-scale network models. Thus, while we considered the effects of field direction and strength on neuronal responses, the modulation that depends on ongoing neuronal activity and their firing patterns should be determined with various stimulus parameters in the future (e.g., stimulus pulse shape and frequency).

Head modeling limitations

We proposed multi-scale models using the head model based on MRI, because this model provides realistic EF distributions that reflect precise underlying anatomy. As the realistic head model can provide accurate analysis, researchers have investigated the influence of the detail of the head model's tissue compartments by including the skull spongiosa or anisotropic white matter's conductivity [6,72,73]. The inclusion of the skull spongiosa changed the EF's orientation, and the white matter anisotropy had limited influence on the EF distributions on the superficial cortical areas, but a greater influence on stimulus-induced current flow oriented parallel to the fiber bundles in the white matter. Therefore, as we found significant dependency of simulated neuronal responses on field orientations, future work should incorporate the detailed head model, especially that with realistic modeling of the skull.

In this study, we constructed the head model via tetrahedral mesh using iso2mesh [37] and Tetgen [38], which has an advantage in its representation of the smooth surface, but is constrained to the closed surface. The realistic head model, which allows intersections between layers and smooth surfaces, can be achieved through the isoparametric geometry-adapted hexahedral finite element approach, resulted in negligible differences in numerical errors with increased modeling accuracy compared to the tetrahedral approach [6,74,75]. As model errors will have a significant influence on the accurate simulation of the EFs [76], sufficiently accurate modeling for realistic EF calculation may be quite beneficial in predicting tES precisely in computational studies.

tES demonstrated variable effects because of the presence of inter-individual differences, and anatomical variation is among the factors that modulate the magnitude of the stimulus-induced field [67,77–81]. Simulation studies that use a head model constructed via MRI are the most cost-effective way to determine NIBS′ effect depending on anatomical variation, because simulated EF can estimate the target areas NIBS affects that reflect individual head model distortion [4,7,22]. For example, Opitz et al. [22] constructed individualized head models for five subjects and then analyzed

simulated field distributions and physiological responses, specifically motor evoked potentials (MEPs), in response to single pulse magnetic stimulation for each subject. They found that magnetic coil orientation with respect to anatomical characteristics of the hand knob affected physiological responses and a correlation between EF strength and MEP amplitudes in the target area. Edwards et al. [78] reported variation in motor excitability with tDCS that resulted in significant inter-individual differences in simulated EF strength and MEP outcomes. These results implied the usefulness of simulation studies to determine customized and individualized parameters of NIBS using individual head models. In addition, Laakso et al. [81] simulated tDCS that targeted the hand area using 24 individual head models and found EF concentrated generally in the perimeter of the ROI and large variation in EF distributions across the models. While the results in this study cannot be generalized, as we used an anatomical head model, we demonstrated the utility of multi-scale modeling during sub- and supra-threshold stimulations. Thus, like Laakso's study, further multi-scale modeling using numerous numbers of individual head models might help improve our understanding of tES at the neuronal level by providing not only individual responses, but also average responses.

Future studies using multi-scale modeling

Most NIBS investigations have focused on the motor cortex because of the clear measurement of outcomes, such as MEP, and thus, other cortical areas have not been investigated fully to date. Although we investigated responses in the motor cortex here, the large-scale modeling of stellate cells and L3 PNs proposed is applicable to targets throughout the cortex, and thus, future studies of non-motor brain areas might help determine NIBS' optimal parameters and potential mechanisms.

Computational studies on tES are designed to determine target brain areas under a myriad of potential montages and we proposed a multi-scale model to predict target brain areas at the neuronal level more precisely. Precise modeling in tES helps achieve accurate calculations of not only realistic EF, but also current injection patterns that optimize tES to maximize the strength and focality of stimulation at the target areas [51,82]. Further, as the reciprocity principle offers a relation between the electroencephalography (EEG) and tES forward modeling approaches [74], the EEG forward problem, which computes the potentials from neural sources at recording electrodes (sensors), was used to determine the optimal current injection patterns required for tES to target neural sources inferred from the EEG [10,11]. These optimization problems in tES were proposed via tES-induced EF using the head model, while we identified the relation between EF and neuronal responses during sub- and supra-threshold stimulations using the multi-scale model. This study suggests that the use of a multi-scale model to determine tES' target areas and thus further analysis of tES forward problems using multi-scale modeling might be helpful in determining optimal tES montages.

Conclusion

We examined the potential relation between the field strength (EF magnitude and its directional components; radial field (RF), and tangential field (TF)) and neuronal responses sub- and supra-threshold stimulations induced using the multi-scale models proposed for tES. We found that RF flowing parallel to the somato-dendritic axis affected neurons' polarizations strongly; sub-threshold RF polarized neurons linearly both under uniform and realistic EFs, while supra-threshold stimulation yielded rather complex patterns of excitation thresholds depending upon the type of neuron. Our results suggested that the stimulus-induced EF's relative direction with respect to cortical neurons and their morphological features are major factors in cortical modulation. Thus, investigation of the directional EF along cortical neurons (for example, RF) may be valuable in future studies of sub-threshold stimulation. In addition, the multi-scale model proposed enables further analysis of compartmental-specific neuronal responses that might help improve inferences about tES's physiological mechanisms [57]. Therefore, multi-scale modeling might offer an improved understanding of tES associated with large combinations of stimulus parameters at the macroscopic and microscopic levels.

Conflicts of interest

We wish to confirm that there are no known conflicts of interest associated with this publication and there has been no significant financial support for this work that could have influenced its outcome. We confirm that the manuscript has been read and approved by all named authors and that there are no other persons who satisfied the criteria for authorship but are not listed. We further confirm that the order of authors listed in the manuscript has been approved by all of us. We confirm that we have given due consideration to the protection of intellectual property associated with this work and that there are no impediments to publication, including the timing of publication, with respect to intellectual property. In so doing we confirm that we have followed the regulations of our institutions concerning intellectual property.

Acknowledgments

This work was supported by the GIST Research Institute (GRI) grant funded by the Gwangju Institute of Science and Technology (GIST) in 2018, the National Research Foundation of Korea (NRF-2016R1A2B4010897, NRF-2018R1D1A1B07041224), and Institute for Information & Communications Technology Promotion (IITP) grant funded by the Korea government (No. 2017-0-00451).

Appendix A. Supplementary data

Supplementary data to this article can be found online at https://doi.org/10.1016/j.brs.2018.11.004.

References

[1] Wagner T, Valero-Cabre A, Pascual-Leone A. Noninvasive human brain stimulation. Annu Rev Biomed Eng 2007;9:527–65. https://doi.org/10.1146/annurev.bioeng.9.061206.133100.

[2] Peterchev AV, Wagner TA, Miranda PC, Nitsche MA, Paulus W, Lisanby SH, et al. Fundamentals of transcranial electric and magnetic stimulation dose: definition, selection, and reporting practices. Brain Stimulat 2012;5:435–53. https://doi.org/10.1016/j.brs.2011.10.001.

[3] Nitsche MA, Cohen LG, Wassermann EM, Priori A, Lang N, Antal A, et al. Transcranial direct current stimulation: state of the art 2008. Brain Stimulat 2008;1:206–23. https://doi.org/10.1016/j.brs.2008.06.004.

[4] Bikson M, Rahman A, Datta A, Fregni F, Merabet L. High-resolution modeling assisted design of customized and individualized transcranial direct current stimulation protocols. Neuromodulation Technol Neural Interface 2012;15:306–15. https://doi.org/10.1111/j.1525-1403.2012.00481.x.

[5] Datta A, Bansal V, Diaz J, Patel J, Reato D, Bikson M. Gyri-precise head model of transcranial direct current stimulation: improved spatial focality using a ring electrode versus conventional rectangular pad. Brain Stimulat 2009;2. https://doi.org/10.1016/j.brs.2009.03.005. 201-207.e1.

[6] Wagner S, Rampersad SM, Aydin Ü, Vorwerk J, Oostendorp TF, Neuling T, et al. Investigation of tDCS volume conduction effects in a highly realistic head model. J Neural Eng 2014;11:016002. https://doi.org/10.1088/1741-2560/11/1/016002.

[7] Windhoff M, Opitz A, Thielscher A. Electric field calculations in brain stimulation based on finite elements: an optimized processing pipeline for the generation and usage of accurate individual head models. Hum Brain Mapp 2013;34:923–35. https://doi.org/10.1002/hbm.21479.

[8] Saturnino GB, Antunes A, Thielscher A. On the importance of electrode parameters for shaping electric field patterns generated by tDCS. Neuroimage 2015;120:25–35. https://doi.org/10.1016/j.neuroimage.2015.06.067.

[9] Opitz A, Paulus W, Will S, Antunes A, Thielscher A. Determinants of the electric field during transcranial direct current stimulation. Neuroimage 2015;109:140–50. https://doi.org/10.1016/j.neuroimage.2015.01.033.

[10] Dmochowski JP, Koessler L, Norcia AM, Bikson M, Parra LC. Optimal use of EEG recordings to target active brain areas with transcranial electrical stimulation. Neuroimage 2017;157:69–80. https://doi.org/10.1016/j.neuroimage.2017.05.059.

[11] Fernández-Corazza M, Turovets S, Luu P, Anderson E, Tucker D. Transcranial electrical neuromodulation based on the reciprocity principle. Front Psychiatr 2016;7. https://doi.org/10.3389/fpsyt.2016.00087.

[12] Korshoej AR, Hansen FL, Thielscher A, Oettingen GB von, Sørensen JCH. Impact of tumor position, conductivity distribution and tissue homogeneity on the distribution of tumor treating fields in a human brain: a computer modeling study. PloS One 2017;12. https://doi.org/10.1371/journal.pone.0179214. e0179214.

[13] Bikson M, Dmochowski J, Rahman A. The "quasi-uniform" assumption in animal and computational models of non-invasive electrical stimulation. Brain Stimulat 2013;6:704–5. https://doi.org/10.1016/j.brs.2012.11.005.

[14] Kamitani Y, Bhalodia VM, Kubota Y, Shimojo S. A model of magnetic stimulation of neocortical neurons. Neurocomputing 2001;38–40:697–703. https://doi.org/10.1016/S0925-2312(01)00447-7.

[15] Rahman A, Reato D, Arlotti M, Gasca F, Datta A, Parra LC, et al. Cellular effects of acute direct current stimulation: somatic and synaptic terminal effects. J Physiol 2013;591:2563–78. https://doi.org/10.1113/jphysiol.2012.247171.

[16] Rattay F. Analysis of models for external stimulation of axons. IEEE Trans Biomed Eng 1986;33:974–7. https://doi.org/10.1109/TBME.1986.325670. BME.

[17] Rattay F. Analysis of models for extracellular fiber stimulation. IEEE Trans Biomed Eng 1989;36:676–82. https://doi.org/10.1109/10.32099.

[18] Rahman A, Lafon B, Bikson M. Chapter 2 - multilevel computational models for predicting the cellular effects of noninvasive brain stimulation. In: Bestmann S, editor. Prog. Brain Res., vol. 222. Elsevier; 2015. p. 25–40. https://doi.org/10.1016/bs.pbr.2015.09.003.

[19] Seo H, Jun SC. Multi-scale computational models for electrical brain stimulation. Front Hum Neurosci 2017;11. https://doi.org/10.3389/fnhum.2017.00515.

[20] Radman T, Ramos RL, Brumberg JC, Bikson M. Role of cortical cell type and morphology in subthreshold and suprathreshold uniform electric field stimulation in vitro. Brain Stimulat 2009;2:215–28. https://doi.org/10.1016/j.brs.2009.03.007. e3.

[21] Nummenmaa A, McNab JA, Savadjiev P, Okada Y, Hämäläinen MS, Wang R, et al. Targeting of white matter tracts with transcranial magnetic stimulation. Brain Stimulat 2014;7:80–4. https://doi.org/10.1016/j.brs.2013.10.001.

[22] Opitz A, Windhoff M, Heidemann RM, Turner R, Thielscher A. How the brain tissue shapes the electric field induced by transcranial magnetic stimulation. Neuroimage 2011;58:849–59. https://doi.org/10.1016/j.neuroimage.2011.06.069.

[23] Shahid SS, Bikson M, Salman H, Wen P, Ahfock T. The value and cost of complexity in predictive modelling: role of tissue anisotropic conductivity and fibre tracts in neuromodulation. J Neural Eng 2014;11, 036002. https://doi.org/10.1088/1741-2560/11/3/036002.

[24] Geeter ND, Dupré L, Crevecoeur G. Modeling transcranial magnetic stimulation from the induced electric fields to the membrane potentials along tractography-based white matter fiber tracts. J Neural Eng 2016;13, 026028. https://doi.org/10.1088/1741-2560/13/2/026028.

[25] Goodwin BD, Butson CR. Subject-specific multiscale modeling to investigate effects of transcranial magnetic stimulation. Neuromodulation Technol Neural Interface 2015;18:694–704. https://doi.org/10.1111/ner.12296.

[26] Salvador R, Silva S, Basser PJ, Miranda PC. Determining which mechanisms lead to activation in the motor cortex: a modeling study of transcranial magnetic stimulation using realistic stimulus waveforms and sulcal geometry. Clin Neurophysiol 2011;122:748–58. https://doi.org/10.1016/j.clinph.2010.09.022.

[27] Seo H, Schaworonkow N, Jun SC, Triesch J. A multi-scale computational model of the effects of TMS on motor cortex. F1000Research 2016;5:1945. https://doi.org/10.12688/f1000research.9277.1.

[28] Seo H, Kim H-I, Jun SC. The effect of a transcranial channel as a skull/brain interface in high-definition transcranial direct current stimulation—a computational study. Sci Rep 2017;7:40612. https://doi.org/10.1038/srep40612.

[29] Wagner T, Rushmore J, Eden U, Valero-Cabre A. Biophysical foundations underlying TMS: setting the stage for an effective use of neurostimulation in the cognitive neurosciences. Cortex 2009;45:1025–34. https://doi.org/10.1016/j.cortex.2008.10.002.

[30] Deng Z-D, Lisanby SH, Peterchev AV. Electric field depth–focality tradeoff in transcranial magnetic stimulation: simulation comparison of 50 coil designs. Brain Stimulat 2013;6:1–13. https://doi.org/10.1016/j.brs.2012.02.005.

[31] Chakraborty D, Truong DQ, Bikson M, Kaphzan H. Neuromodulation of axon terminals. Cereb Cortex n.d.:1–9.http://doi.org/10.1093/cercor/bhx158.

[32] Yi G-S, Wang J, Deng B, Wei X-L. Morphology controls how hippocampal CA1 pyramidal neuron responds to uniform electric fields: a biophysical modeling study. Sci Rep 2017;7:3210. https://doi.org/10.1038/s41598-017-03547-6.

[33] Thielscher A, Antunes A, Saturnino GB. Field modeling for transcranial magnetic stimulation: a useful tool to understand the physiological effects of TMS?. In: 2015 37th Annu Int Conf IEEE Eng Med Biol Soc EMBC; 2015. https://doi.org/10.1109/EMBC.2015.7318340. 222–5.

[34] Dale AM, Fischl B, Sereno MI. Cortical surface-based analysis: I. Segmentation and surface reconstruction. Neuroimage 1999;9:179–94. https://doi.org/10.1006/nimg.1998.0395.

[35] Fischl B, Sereno MI, Dale AM. Cortical surface-based analysis: II: inflation, flattening, and a surface-based coordinate system. Neuroimage 1999;9:195–207. https://doi.org/10.1006/nimg.1998.0396.

[36] Smith SM, Jenkinson M, Woolrich MW, Beckmann CF, Behrens TEJ, Johansen-Berg H, et al. Advances in functional and structural MR image analysis and implementation as FSL. Neuroimage 2004;23(Supplement 1):S208–19. https://doi.org/10.1016/j.neuroimage.2004.07.051.

[37] Fang Q, Boas DA. Tetrahedral mesh generation from volumetric binary and grayscale images. In: IEEE Int. Symp. Biomed. Imaging Nano Macro 2009 ISBI 09; 2009. p. 1142–5. https://doi.org/10.1109/ISBI.2009.5193259.

[38] Si H. TetGen, a delaunay-based quality tetrahedral mesh generator. ACM Trans Math Software 2015;41. https://doi.org/10.1145/2629697. 11:1–11:36.

[39] Rampersad SM, Janssen AM, Lucka F, Aydin Ü, Lanfer B, Lew S, et al. Simulating transcranial direct current stimulation with a detailed anisotropic human head model. IEEE Trans Neural Syst Rehabil Eng 2014;22:441–52. https://doi.org/10.1109/TNSRE.2014.2308997.

[40] Wagner T, Fregni F, Fecteau S, Grodzinsky A, Zahn M, Pascual-Leone A. Transcranial direct current stimulation: a computer-based human model study. Neuroimage 2007;35:1113–24. https://doi.org/10.1016/j.neuroimage.2007.01.027.

[41] Thielscher A, Opitz A, Windhoff M. Impact of the gyral geometry on the electric field induced by transcranial magnetic stimulation. Neuroimage 2011;54:234–43. https://doi.org/10.1016/j.neuroimage.2010.07.061.

[42] Wagner TA, Zahn M, Grodzinsky AJ, Pascual-Leone A. Three-dimensional head model Simulation of transcranial magnetic stimulation. IEEE Trans Biomed Eng 2004;51:1586–98. https://doi.org/10.1109/TBME.2004.827925.

[43] Mainen ZF, Sejnowski TJ. Influence of dendritic structure on firing pattern in model neocortical neurons. Nature 1996;382:363–6. https://doi.org/10.1038/382363a0.

[44] Hines ML, Carnevale NT. The NEURON simulation environment. Neural Comput 1997;9:1179–209. https://doi.org/10.1162/neco.1997.9.6.1179.

[45] Wongsarnpigoon A, Grill WM. Computer-based model of epidural motor cortex stimulation: effects of electrode position and geometry on activation of cortical neurons. Clin Neurophysiol 2012;123:160–72. https://doi.org/10.1016/j.clinph.2011.06.005.

[46] Seo H, Kim D, Jun SC. Effect of anatomically realistic full-head model on activation of cortical neurons in subdural cortical stimulation—a computational study. Sci Rep 2016;6:27353. https://doi.org/10.1038/srep27353.

[47] DeFelipe J, Alonso-Nanclares L, Arellano JI. Microstructure of the neocortex: comparative aspects. J Neurocytol 2002;31:299–316. https://doi.org/10.1023/A:1024130211265.

[48] Mountcastle VB. The columnar organization of the neocortex. Brain 1997;120:701–22. https://doi.org/10.1093/brain/120.4.701.

[49] Parazzini M, Fiocchi S, Ravazzani P. Electric field and current density distribution in an anatomical head model during transcranial direct current stimulation for tinnitus treatment. Bioelectromagnetics 2012;33:476–87. https://doi.org/10.1002/bem.21708.

[50] Shahid S, Wen P, Ahfock T. Assessment of electric field distribution in anisotropic cortical and subcortical regions under the influence of tDCS. Bioelectromagnetics 2014;35:41–57. https://doi.org/10.1002/bem.21814.

[51] Dmochowski JP, Datta A, Bikson M, Su Y, Parra LC. Optimized multi-electrode stimulation increases focality and intensity at target. J Neural Eng 2011;8, 046011. https://doi.org/10.1088/1741-2560/8/4/046011.

[52] Bikson M, Inoue M, Akiyama H, Deans JK, Fox JE, Miyakawa H, et al. Effects of uniform extracellular DC electric fields on excitability in rat hippocampal slices in vitro. J Physiol 2004;557:175–90. https://doi.org/10.1113/jphysiol.2003.055772.

[53] Chan CY, Nicholson C. Modulation by applied electric fields of Purkinje and stellate cell activity in the isolated turtle cerebellum. J Physiol 1986;371:89–114.

[54] Purpura DP, McMurtry JG. Intracellular activities and evoked potential changes during polarization of motor cortex. J Neurophysiol 1965;28:166–85. https://doi.org/10.1152/jn.1965.28.1.166.

[55] Bindman LJ, Lippold OCJ, Redfearn JWT. The action of brief polarizing currents on the cerebral cortex of the rat (1) during current flow and (2) in the production of long-lasting after-effects. J Physiol 1964;172:369–82. https://doi.org/10.1113/jphysiol.1964.sp007425.

[56] Nitsche MA, Paulus W. Noninvasive brain stimulation protocols in the treatment of epilepsy: current state and perspectives. Neurotherapeutics 2009;6:244–50. https://doi.org/10.1016/j.nurt.2009.01.003.

[57] Ranck JB. Which elements are excited in electrical stimulation of mammalian central nervous system: a review. Brain Res 1975;98:417–40. https://doi.org/10.1016/0006-8993(75)90364-9.

[58] Wu T, Fan J, Lee KS, Li X. Cortical neuron activation induced by electromagnetic stimulation: a quantitative analysis via modelling and simulation. J Comput Neurosci 2016;40:51–64. https://doi.org/10.1007/s10827-015-0585-1.

[59] Manola L, Roelofsen BH, Holsheimer DJ, Marani E, Geelen J. Modelling motor cortex stimulation for chronic pain control: electrical potential field, activating functions and responses of simple nerve fibre models. Med Biol Eng Comput 2005;43:335–43. https://doi.org/10.1007/BF02345810.
[60] Manola L, Holsheimer J, Veltink P, Buitenweg JR. Anodal vs cathodal stimulation of motor cortex: a modeling study. Clin Neurophysiol 2007;118:464–74. https://doi.org/10.1016/j.clinph.2006.09.012.
[61] Zwartjes DGM, Heida T, Feirabend HKP, Janssen MLF, Visser-Vandewalle V, Martens HCF, et al. Motor cortex stimulation for Parkinson's disease: a modelling study. J Neural Eng 2012;9, 056005. https://doi.org/10.1088/1741-2560/9/5/056005.
[62] Geeter ND, Crevecoeur G, Leemans A, Dupré L. Effective electric fields along realistic DTI-based neural trajectories for modelling the stimulation mechanisms of TMS. Phys Med Biol 2015;60:453. https://doi.org/10.1088/0031-9155/60/2/453.
[63] Nolte J. The human brain: an introduction to its functional anatomy. Mosby; 2002.
[64] Lei W, Jiao Y, Mar ND, Reiner A. Evidence for differential cortical input to direct pathway versus indirect pathway striatal projection neurons in rats. J Neurosci 2004;24:8289–99. https://doi.org/10.1523/JNEUROSCI.1990-04.2004.
[65] Buxhoeveden DP, Casanova MF. The minicolumn hypothesis in neuroscience. Brain 2002;125:935–51. https://doi.org/10.1093/brain/awf110.
[66] Silva S, Basser PJ, Miranda PC. Elucidating the mechanisms and loci of neuronal excitation by transcranial magnetic stimulation using a finite element model of a cortical sulcus. Clin Neurophysiol 2008;119:2405–13. https://doi.org/10.1016/j.clinph.2008.07.248.
[67] Dayan E, Censor N, Buch ER, Sandrini M, Cohen LG. Noninvasive brain stimulation: from physiology to network dynamics and back. Nat Neurosci 2013;16:838. https://doi.org/10.1038/nn.3422.
[68] Esser SK, Hill SL, Tononi G. Modeling the effects of transcranial magnetic stimulation on cortical circuits. J Neurophysiol 2005;94:622–39. https://doi.org/10.1152/jn.01230.2004.
[69] Rusu CV, Murakami M, Ziemann U, Triesch J. A model of TMS-induced I-waves in motor cortex. Brain Stimulat 2014;7:401–14. https://doi.org/10.1016/j.brs.2014.02.009.
[70] Abdeen MA, Stuchly MA. Modeling of magnetic field stimulation of bent neurons. IEEE Trans Biomed Eng 1994;41:1092–5. https://doi.org/10.1109/10.335848.
[71] Maccabee PJ, Amassian VE, Eberle LP, Cracco RQ. Magnetic coil stimulation of straight and bent amphibian and mammalian peripheral nerve in vitro: locus of excitation. J Physiol 1993;460:201–19. https://doi.org/10.1113/jphysiol.1993.sp019467.
[72] Suh HS, Lee WH, Kim T-S. Influence of anisotropic conductivity in the skull and white matter on transcranial direct current stimulation via an anatomically realistic finite element head model. Phys Med Biol 2012;57:6961. https://doi.org/10.1088/0031-9155/57/21/6961.
[73] Vorwerk J, Cho J-H, Rampp S, Hamer H, Knösche TR, Wolters CH. A guideline for head volume conductor modeling in EEG and MEG. Neuroimage 2014;100:590–607. https://doi.org/10.1016/j.neuroimage.2014.06.040.
[74] Wagner S, Lucka F, Vorwerk J, Herrmann CS, Nolte G, Burger M, et al. Using reciprocity for relating the simulation of transcranial current stimulation to the EEG forward problem. Neuroimage 2016;140:163–73. https://doi.org/10.1016/j.neuroimage.2016.04.005.
[75] Wolters CH, Anwander A, Berti G, Hartmann U. Geometry-adapted hexahedral meshes improve accuracy of finite-element-method-based EEG source analysis. IEEE Trans Biomed Eng 2007;54:1446–53. https://doi.org/10.1109/TBME.2007.890736.
[76] Vorwerk J, Clerc M, Burger M, Wolters CH. Comparison of boundary element and finite element approaches to the EEG forward problem. Biomed Eng Biomed Tech 2012;57:795–8. https://doi.org/10.1515/bmt-2012-4152.
[77] Datta A, Truong D, Minhas P, Parra LC, Bikson M. Inter-individual variation during transcranial direct current stimulation and normalization of dose using MRI-derived computational models. Front Psychiatr 2012;3. https://doi.org/10.3389/fpsyt.2012.00091.
[78] Edwards D, Cortes M, Datta A, Minhas P, Wassermann EM, Bikson M. Physiological and modeling evidence for focal transcranial electrical brain stimulation in humans: a basis for high-definition tDCS. Neuroimage 2013;74:266–75. https://doi.org/10.1016/j.neuroimage.2013.01.042.
[79] Li LM, Uehara K, Hanakawa T. The contribution of interindividual factors to variability of response in transcranial direct current stimulation studies. Front Cell Neurosci 2015;9. https://doi.org/10.3389/fncel.2015.00181.
[80] Opitz A, Legon W, Rowlands A, Bickel WK, Paulus W, Tyler WJ. Physiological observations validate finite element models for estimating subject-specific electric field distributions induced by transcranial magnetic stimulation of the human motor cortex. Neuroimage 2013;81:253–64. https://doi.org/10.1016/j.neuroimage.2013.04.067.
[81] Laakso I, Hirata A, Ugawa Y. Effects of coil orientation on the electric field induced by TMS over the hand motor area. Phys Med Biol 2014;59:203. https://doi.org/10.1088/0031-9155/59/1/203.
[82] Ruffini G, Fox MD, Ripolles O, Miranda PC, Pascual-Leone A. Optimization of multifocal transcranial current stimulation for weighted cortical pattern targeting from realistic modeling of electric fields. Neuroimage 2014;89:216–25. https://doi.org/10.1016/j.neuroimage.2013.12.002.